Journal of Ceramic Processing Research. Vol. 26, No. 2, pp. 203~208 (2025)
(Received 1 November 2024, Received in revised form 21 February 2025, Accepted 1 March 2025)
https://doi.org/10.36410/jcpr.2025.26.2.203

J O U R N A L O F
Ceramic Processing Research

Effect of Nb doping on the microstructure and DC electrical conductivity of nickel ferrite ceramics

Baogang Liu*, Jingyao Xia, Yang Yu and Huixin Liu
School of Energy and Electromechanical Engineering, Hunan University of Humanities, Science and Technology, Loudi 417000, China

Research on the performance of nickel ferrite ceramics is significant for the practical application. This study prepared $Ni_{1-x}Nb_xFe_2O_4$ ceramics (x = 0, 0.02, 0.05, 0.07, 0.10, 0.20) via a solid state reaction, and analyzed how Nb doping affected phase compositions, grain sizes, relative densities as well as DC conductivities was investigated. The results showed that the $Ni_{1-x}Nb_xFe_2O_4$ ceramics contained both $NiFe_2O_4$ and NiO phases when the Nb doping amount x was less than 0.20. The grain sizes of the $Ni_{1-x}Nb_xFe_2O_4$ ceramics slowly elevated as the Nb doping amount elevated. The mean grain size of around 50 μm was obtained at the doping amount x of 0.20, 2.5 times higher than that of undoped $NiFe_2O_4$ ceramics. The relative densities and DC conductivities of the $Ni_{1-x}Nb_xFe_2O_4$ ceramics first increased and then decreased gradually with the increase of Nb doping amount. When the Nb doping amount x was 0.05, the relative densities and DC conductivities reached the maximum, which were 99.35% and 36.37 S/cm (960 °C), respectively. The factors affecting the microstructure and DC electrical conductivities of the $Ni_{1-x}Nb_xFe_2O_4$ ceramics were also discussed in detail.

Keywords: Microstructure, Electrical conductivity, Nickel ferrite, Ceramics.

Introduction

Nickel ferrite is considered a very attractive material because of its unique properties and practical applications [1, 2]. It is widely used in various areas, like supercapacitor [3], data storage [4], catalysts [5], H_2O decomposition [6], ferrofluids [7], gas sensors [8], inert anodes [9], magnetic drug delivery [10], glycan analysis [11] and microwave absorbers [12]. The microstructure and electrical conductivity of nickel ferrite ceramics is significant for the applications. Therefore, numerous researchers have carried out extensive research and discussion on this issue. Hassan et al. prepared Al substituted Ni ferrites successfully as energy storage devices [13]. They found that the Al substituted Ni ferrites had increased DC electrical resistivity as Al content elevated within the samples, making the material suitable for high frequency applications. Kamar, et al. synthesized four nickel ferrite powder samples of diverse nanoparticle sizes and morphologies, and studied how particle size and morphology affected electrical performances of $NiFe_2O_4$ nanoparticles [14]. Anu et al. analyzed how Zn doping affected electrical property of $NiFe_2O_4$ nanoparticles. The results showed that the nanoparticles with critical dopant concentration exhibited higher values of electrical conductivity because of the increased Fe^{3+} ion hopping at octahedral sites [15]. In our previous research, we found that the relative density and DC conductivity of nickel ferrite ceramics sintered under the nitrogen atmosphere dramatically elevated in comparison with those sintered in air [16]. Doping can effectively enhance the relative density and electrical conductivity of nickel ferrite ceramics. Given the facts that the radius of Nb^{5+} is relatively closer to that of Ni^{2+}, it could be deduced that Nb atoms could intercalate into the crystal lattice of $NiFe_2O_4$ ceramics by partial replacement of Ni atoms [17]. In this work, $Ni_{1-x}Nb_xFe_2O_4$ ceramics (x = 0, 0.02, 0.05, 0.07, 0.10, 0.20) were prepared via traditional powder metallurgy process and sintered under nitrogen at the initial oxygen partial pressure being ~100 ppm, so as to analyze how Nb doping affected the microstructure and DC electrical conductivities of nickel ferrite.

Experimental

$Ni_{1-x}Nb_xFe_2O_4$ ceramics (x = 0, 0.02, 0.05, 0.07, 0.10, 0.20) were prepared via a solid state reaction according to the stoichiometry ratio. The high-purity NiO (99.8%, Jinchuan, China), Nb_2O_5 (99.5%, Shanghai, China) and Fe_2O_3 (99.8%, Qidong, China) were used to be raw materials. After weighing, the powder underwent 4 h of wet ball-milling within distilled water with WC-8Co cemented carbide balls, at the ball-to-powder mass ratio of 3:1, with polyvinyl alcohol (PVA) being the binder.

*Corresponding author:
Tel : (86-738)8326910
Fax: (86-738)8326910
E-mail: liudd2016@126.com

This resultant mixed sample was heated for 24 hours under 100 ºC, followed by 6 h of calcination under 1200 °C within a muffle furnace. The calcined powder was later subjected to uniaxial compaction at 120 MPa for forming the cylindrical blocks, and later 4 h of sintering under 1300 °C under nitrogen, and the initial oxygen partial pressure was ~100 ppm. After firing, the samples underwent cooling at 0.5 °C/min for avoiding thermal shock-induced cracking.

The phase compositions of $Ni_{1-x}Nb_xFe_2O_4$ ceramics were detected by X-ray diffraction (Dmax/2550VB+, Tokyo, Japan) under Cu-Kα radiation. The $Ni_{1-x}Nb_xFe_2O_4$ ceramics microstructures were analyzed with the use of scanning electron microscopy (Hitachi S-4800, Tokyo, Japan). Archimedes approach was adopted for measuring bulk densities. Also, DC electrical conductivity was calculated at 300-960 °C through the four-point probe approach. Among them, two probes were applied in supplying current, whereas the other two were adopted for measuring voltage.

Results and Discussion

Phase composition

Fig. 1 displays X-ray diffraction patterns for samples with compositions of $Ni_{0.98}Nb_{0.02}Fe_2O_4$ and $Ni_{0.80}Nb_{0.20}Fe_2O_4$ sintered at 1300 °C under nitrogen atmosphere. It could be observed that at low doping concentrations of Nb_2O_5, the samples predominantly exhibited two phases: $NiFe_2O_4$ and NiO, with no detectable diffraction peaks corresponding to Nb-containing compounds. However, at a doping concentration of x = 0.20, weaker intensity diffraction peaks of $FeNbO_4$ emerged in the samples, while the diffraction peaks associated with the NiO phase were no longer present.

Fig. 2 shows the SEM morphology of $Ni_{1-x}Nb_xFe_2O_4$ ceramics sintered at 1300 °C under nitrogen atmosphere

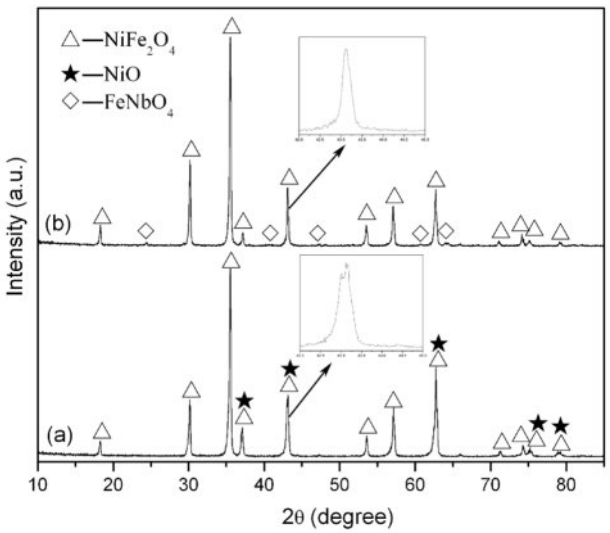

Fig. 1. X-ray diffraction patterns of $Ni_{1-x}Nb_xFe_2O_4$ ceramics sintered at 1300 °C: (a) x = 0.02; (b) x = 0.20.

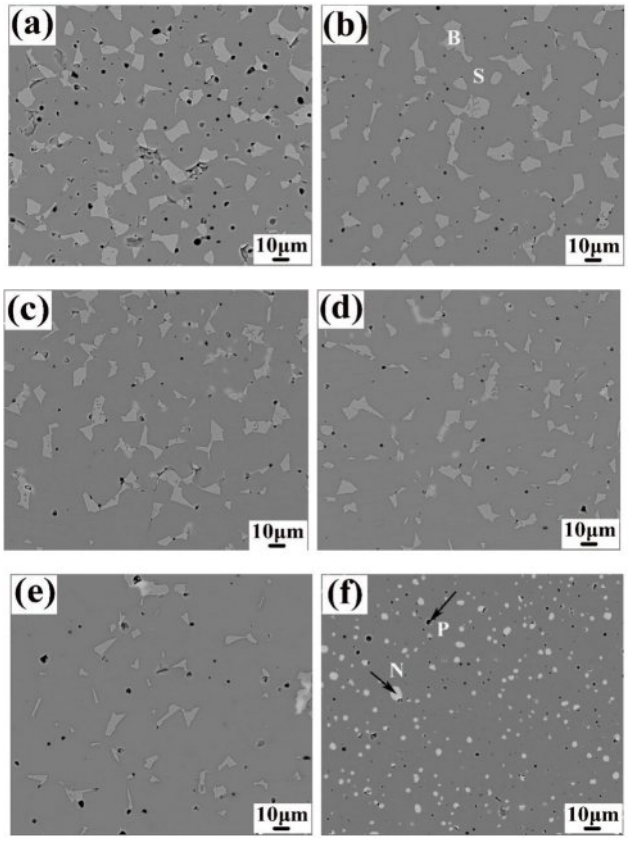

Fig. 2. SEM images of polished $Ni_{1-x}Nb_xFe_2O_4$ ceramics sintered at 1300 °C: (a) x = 0.00; (b) x = 0.02; (c) x = 0.05; (d) x = 0.07; (e) x = 0.10; (f) x = 0.20. Legend: S = spinel, B = bunsenite, N = $FeNbO_4$, and P = pores.

after polishing. It was evident that the number of holes in the doped samples was significantly reduced, resulting in increased density. As the concentration of Nb_2O_5 doping increased, the NiO phase in the samples diminished until it was no longer detectable. At x = 0.20, a white, speckled $FeNbO_4$ phase emerged in the samples, which aligned with the analytical results obtained from X-ray diffraction (XRD) presented in Fig. 1. Table 1 presents EDX analysis of spinel phase of $Ni_{1-x}Nb_xFe_2O_4$ ceramics. It was evident that as the Nb content increased, the Ni content within the $NiFe_2O_4$ ceramic spinel phase continued to rise, even though the Ni content in the sample's composition ratio decreased. This showed that Nb_2O_5 doping could inhibit the dissociation of $NiFe_2O_4$ ceramics to NiO in nitrogen atmosphere. The ionic radii of Nb^{5+} and Ni^{2+} were comparable, both measuring 0.69 Å. However, Nb^{5+} possessed a higher cationic valence, resulting in a more tremendous bonding energy for Nb-O ionic bonds compared to Ni-O ionic bonds. Consequently, Nb-O bonds exhibited greater strength than Ni-O bonds. When Nb^{5+} partially substituted Ni^{2+} within the lattice of $NiFe_2O_4$ ceramics, it could effectively reduce the oxygen ion vacancy concentration within the lattice. This reduction enhanced the stability of the spinel structure of $NiFe_2O_4$ ceramics, thereby inhibiting the dissociation

Table 1. EDX analysis in the spinel phase of $Ni_{1-x}Nb_xFe_2O_4$ ceramics.

Nb content x	Ni/at%	Fe/at%	Nb/at%	O/at%
x = 0.00	10.63	34.19	0.00	55.18
x = 0.02	10.59	33.11	0.42	55.88
x = 0.05	10.62	32.32	1.06	56.00
x = 0.07	11.04	31.53	1.37	56.05
x = 0.10	11.32	31.27	2.01	55.40
x = 0.20	11.55	29.55	2.64	56.26

of $NiFe_2O_4$ [18].

Grain sizes

Fig. 3 displays SEM morphology of $Ni_{0.95}Nb_{0.05}Fe_2O_4$ and $Ni_{0.90}Nb_{0.10}Fe_2O_4$ ceramic powders obtained by calcination at 1200 °C in air. It could be seen that the doped $NiFe_2O_4$ ceramic powders were well crystallized, with a slight agglomeration phenomenon between the particles and the mean power grain size of about 2.5 μm.

Fig. 4 shows the SEM morphology of $Ni_{1-x}Nb_xFe_2O_4$ (x = 0, 0.02, 0.05, 0.07, 0.10, 0.20) ceramic fracture sintered at 1300 °C under nitrogen atmosphere. It could be found that $NiFe_2O_4$ ceramics had gradually increased grain size as Nb_2O_5 doping elevated. The mean grain size of the undoped samples was about 20 μm, and when the doping amount x = 0.20, grain size reached about 50 μm. This phenomenon could be explained by the following reasons. First of all, Nb^{5+} ions possessed a higher cationic valence as compared to Ni^{2+} ions. when Nb^{5+} replaced Ni^{2+} into the lattice of $NiFe_2O_4$ ceramics, the cationic vacancies of Ni^{2+} and Fe^{3+} were formed in the lattice in order to maintain the balance of valences. The concentration of these cationic vacancies increased as doping amount elevated. The increasing cation vacancy concentration accelerated the migration rate of grain boundaries and pores, resulting in continuous grain growth. In addition, the previous analysis indicated that the NiO phase in the $NiFe_2O_4$ ceramic samples decreased continuously with the increase of Nb_2O_5 doping amount. The NiO phase as the second phase hindered the migration of grain boundaries. Therefore,

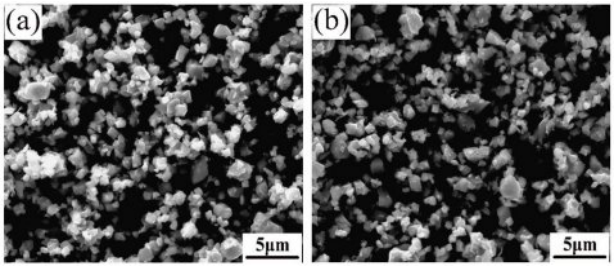

Fig. 3. SEM images of $Ni_{1-x}Nb_xFe_2O_4$ powders calcined at 1200 °C: (a) x = 0.05; (b) x = 0.10.

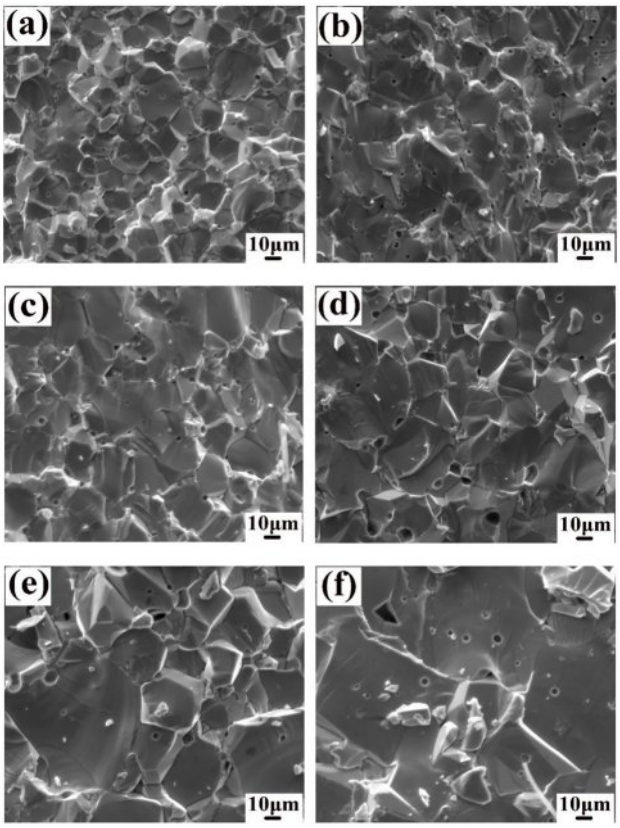

Fig. 4. Cross-section SEM images of $Ni_{1-x}Nb_xFe_2O_4$ ceramics sintered at 1300 °C: (a) x = 0.00; (b) x = 0.02; (c) x = 0.05; (d) x = 0.07; (e) x = 0.10; (f) x = 0.20.

the reduction in the number of NiO phase was also an important reason for promoting the continuous growth of grains with the increase of doping amount.

Relative densities

It could be seen from Fig. 2 that the pores of $NiFe_2O_4$ ceramics were reduced after doping Nb_2O_5, and the samples became very dense. For investigating how Nb_2O_5 doping affected sintering properties of $NiFe_2O_4$ ceramics, relative densities and porosities of the samples with different doping amounts were computed (Table 2). Clearly, the lattice constants of $NiFe_2O_4$ ceramics exhibited minimal variation after Nb_2O_5 doping, primarily due to the same ionic radius between Nb^{5+} and Ni^{2+} [19-21]. The relative densities of $NiFe_2O_4$ ceramics increased and then decreased as Nb_2O_5 doping increased, and relative densities peaked at 99.35% when Nb Nb doping amount x was 0.05. According to the sintering mechanism, ceramic sample sintering was mainly attained through cation and anion diffusion, and their diffusion rates together decided the sample sintering properties [22]. $NiFe_2O_4$ was classified as the inverse spinel structure wherein the lattice was densely packed with oxygen ions, and the metal cations were filled in the in the tetrahedral and octahedral interstices. The diffusion rate of each ion was closely

Table 2. Relative densities of $Ni_{1-x}Nb_xFe_2O_4$ ceramics sintered in nitrogen at 1300 °C.

Nb content x	Lattice parameter a (Å)	X-ray density Dx (g/cm^3)	Bulk density D (g/cm^3)	Relative density (%)	Porosity (%)
0.00	8.358	5.33	5.15	96.62	3.38
0.02	8.359	5.35	5.214	97.46	2.54
0.05	8.357	5.37	5.335	99.35	0.65
0.07	8.364	5.38	5.232	97.25	2.75
0.10	8.369	5.39	5.224	96.92	3.08

related to its vacancy concentration. The higher the ion vacancy concentration, the greater the diffusion rate [23, 24]. For the $Ni_{1-x}Nb_xFe_2O_4$ series ceramics, all samples were sintered under nitrogen atmosphere. The effect of vacancy concentration and the diffusion rate of oxygen ions on the sample relative densities was basically the same. The primary reason for the difference in relative densities was the vacancy concentration and the diffusion rate of metal cations. Compared to Ni^{2+} ions, Nb^{5+} ions had higher cation valence. When Nb^{5+} replaced Ni^{2+} into the lattice of $NiFe_2O_4$ ceramics, cation vacancies of Ni^{2+} and Fe^{3+} were formed in order to maintain charge balance, and the concentration of these cation vacancies increased with higher doping. According to the sintering mechanism [22], the increase of the cation vacancy concentration of Ni^{2+} and Fe^{3+} was conducive to improving the diffusion rate of the corresponding ions, and the sample relative densities eventually elevated with the increase of the doping amount of Nb_2O_5. However, as Nb_2O_5 doping further increased, the increasing cation vacancy concentration increased the moving speed of the grain boundaries, resulting in the growth rate of grains too fast so that the pores could not be eliminated in time and remained in the grains, as shown in Fig. 4(f). As a result, the relative densities of the materials showed a downward trend.

Electrical conductivity

Fig. 5 displays the changes in electrical conductivities at the $Ni_{1-x}Nb_xFe_2O_4$ ceramics sintering temperature of 1300 °C under nitrogen atmosphere. It could be seen that the sample electrical conductivities elevated with rising temperature, showing the conduction law of semiconductor. The DC conductivities of the $Ni_{1-x}Nb_xFe_2O_4$ ceramics first elevated and later declined as Nb doping amount increased. The x = 0.05 composition showed the highest conductivity of the series with a value of 36.37 S/cm at 960 °C, which increased by 60.5% compared to undoped $NiFe_2O_4$ ceramics. In order to analyze the concentration of Fe^{2+} at the octahedral and and the valence of the Nb in $NiFe_2O_4$ ceramics doped with Nb_2O_5, XPS tests were performed on the samples with compositions of $NiFe_2O_4$ and $Ni_{0.95}Nb_{0.05}Fe_2O_4$. Fig. 6 shows the XPS spectras of the Fe_2p peaks of the two samples. $Fe^{3+}{}_A$ represents Fe^{3+} at the A position of the

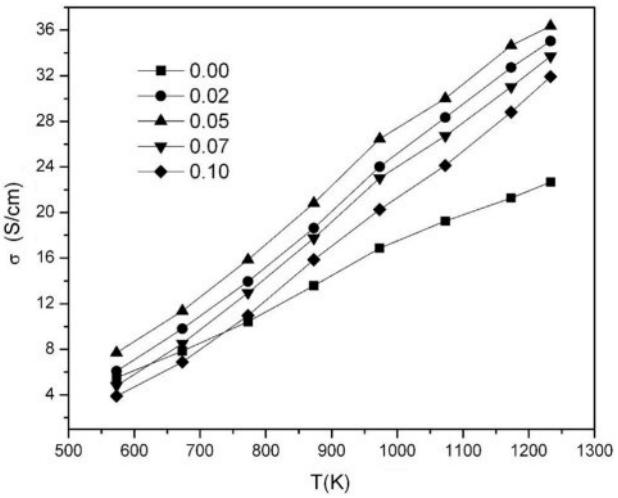

Fig. 5. Plots of σ vs. T for $Ni_{1-x}Nb_xFe_2O_4$ ceramics sintered at 1300 °C.

spinel tetrahedron, $Fe^{3+}{}_B$ and $Fe^{2+}{}_B$ represent Fe^{3+} and Fe^{2+} at the B position of the octahedron, and S1 and S2 are satellite peaks, respectively. It could be seen that the element Fe in both samples presented two valence states of +3 and +2. The corresponding peak positions, peak areas, and the ratios of octahedral Fe^{2+}/Fe^{3+} for each peak were shown in Table 3. It could be observed that the ratios of Fe^{2+}/Fe^{3+} at octahedral positions in the doped samples increased by 3.9% compared with undoped samples. After Nb^{5+} replaced Ni^{2+} into the lattice of $NiFe_2O_4$ ceramics, some Fe^{3+} were reduced to Fe^{2+} for maintaining the valence balance, and the generated Fe^{2+} preferentially occupied the B-position of the octahedron [25, 26], resulting in the increase of $Fe^{2+}{}_B/Fe^{3+}{}_B$ in the B-position of the octahedron (see Table 3).

The electrical conductivity of $NiFe_2O_4$ ceramics depended on the concentration of Fe^{2+} at octahedral sites [27, 28]. The higher concentration of Fe^{2+} led to the superior material electrical conductivity. Thus, the increase of Fe^{2+}/Fe^{3+} ratio after doping made $NiFe_2O_4$ ceramics exhibit more excellent electrical conductivity. The Nb^{5+} ions into the lattice also resulted in octahedral B-site Fe^{3+} vacancies, and the concentration of these vacancies increased as Nb_2O_5 doping amount increased. The increasing Fe^{3+} vacancy concentration reduced the

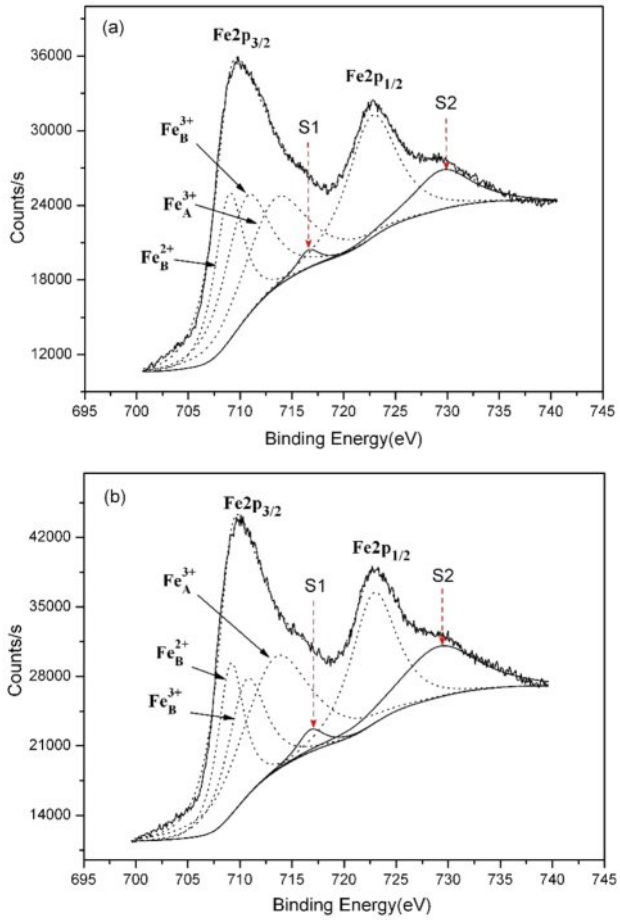

Fig. 6. XPS spectrums of Fe2p peaks for $Ni_{1-x}Nb_xFe_2O_4$ samples sintered at 1300 °C: (a) x = 0.00; (b) x = 0.05.

probability of electron hopping between octahedral Fe^{2+} and Fe^{3+} ions. Therefore, the $NiFe_2O_4$ ceramics conductivities showed a decreasing trend when the doping amount exceeded 0.05. In addition, the relative densities of doped $NiFe_2O_4$ ceramics exhibited the similar trend to that of the electrical conductivity, both increasing initially and then decreasing, peaking at x = 0.05. The increasing relative density could reduce the electron transport resistance [29], so the effect of the relative densities of doped $NiFe_2O_4$ ceramics on the electrical conductivity could not be overlooked.

Fig. 7 shows the plots of lnσ vs. 1000/T for $Ni_{1-x}Nb_xFe_2O_4$ ceramics sintered at 1300 °C. Solid lines were fitted to the data according to the Arrhenius equation. The activation energy ΔE and the R^2 value were obtained in Table 4 from the slopes of the fitted

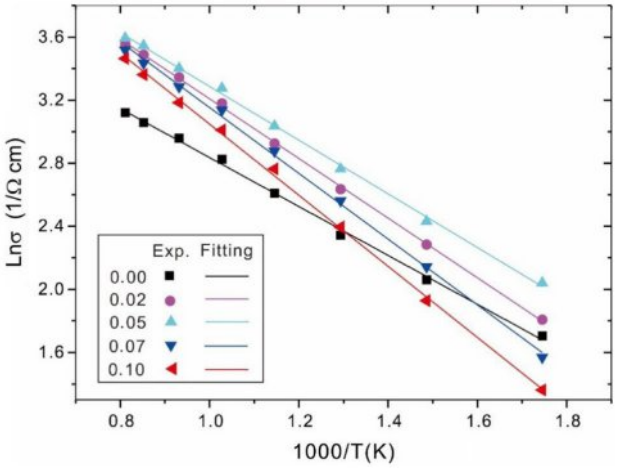

Fig. 7. Plots of lnσ vs. 1000/T for $Ni_{1-x}Nb_xFe_2O_4$ ceramics sintered at 1300 °C. Solid lines were fitted to the data according to the Arrhenius equation.

Table 4. Conduction activation energy ΔE and R^2 value for $Ni_{1-x}Nb_xFe_2O_4$ samples sintered in nitrogen at 1300 °C.

Nb content x	ΔE (eV)	R^2
0.00	0.134	0.00385
0.02	0.163	0.00120
0.05	0.147	0.00339
0.07	0.179	0.00549
0.10	0.194	0.00401

lines. It could be seen that for all the prepared samples, there was basically a linear relationship between lnσ and 1000/T, indicating that the relationship between the electrical conductivity and temperature in the doped samples remained consistent with $\sigma = \sigma_0 \exp[-(\Delta E/kT)]$. In addition, as shown in Table 4, the doping concentration (x = 0.05) corresponded to the lowest conductive activation energy in the doped samples. The observed inverse correlation between activation energy and electrical conductivity was in good agreement with the fundamental semiconductor theory, where lower activation energies typically correspond to higher charge carrier mobility and improved conductivity performance.

Conclusions

In this work, the microstructures, phase compositions, grain sizes, relative densities as well as electrical

Table 3. Relative datas of Fe2p peaks for $Ni_{1-x}Nb_xFe_2O_4$ samples sintered at 1300 °C.

Nb content	Peak position (eV)			Peak area (eV/s)			Fe^{2+}_B/Fe^{3+}_B
x	Fe^{2+}_B	Fe^{3+}_B	Fe^{3+}_A	Fe^{2+}_B	Fe^{3+}_B	Fe^{3+}_A	(%)
0.00	708.9	710.6	713.4	46770	59302	59525	44.1
0.05	709.1	710.6	713.4	54941	59637	106210	48.0

conductivities of Nb doped nickel ferrite ceramics were studied. According to our obtained experimental analysis, we could draw three conclusions below.

(1) When the Nb doping amount x was less than 0.20, only diffraction peaks of $NiFe_2O_4$ and NiO could be detected in $Ni_{1-x}Nb_xFe_2O_4$ ceramics. On the contrary, when the Nb doping amount x was 0.20, the diffraction peak of $FeNbO_4$ appeared while the diffraction peak of NiO phase gradually disappeared.

(2) The grain sizes of the $Ni_{1-x}Nb_xFe_2O_4$ ceramics slowly elevated as Nb doping amount elevated. At the doping amount x of 0.20, the mean grain size reached around 50 μm, 2.5 times higher than that of undoped $NiFe_2O_4$ ceramics. This was associated with the increasing speed of grain boundary movement and the increase of the pore mobility.

(3) when the Nb doping amount x was 0.05, the relative densities reached the maximum value of 99.35%, which increased by 2.73% compared to pure $NiFe_2O_4$ samples, attributing to the increase of Ni^{2+} and Fe^{3+} vacancy concentration.

(4) The DC conductivities of the $Ni_{1-x}Nb_xFe_2O_4$ ceramics first elevated and later declined as the Nb doping amount elevated. The x = 0.05 composition showed the highest conductivity of the series with a value of 36.37 S/cm at 960 °C, which increased by 60.5% compared to undoped $NiFe_2O_4$ ceramics. It was because that Fe^{2+} ion concentration elevated at the octahedral sites after Nb doping and the porosity decreased.

Acknowledgements

This study was funded by the Scientific Research Fund of Hunan Provincial Education Department (23A0614), the Hunan Provincial Natural Science Foundation of China (2024JJ7262) and the Double First-Class Discipline Construction Program of Hunan Province.

References

1. H.Y. He, J. Ceram. Process. Res. 16 (2015) 313.
2. Q. Liu, L. Lv, J. Zhou, X. Chen, X. Bian, and P. Liu, J. Ceram. Process. Res. 13 (2012) 110.
3. B. Dey, C. Manoharan, M. Venkateshwarlu, C.S. Pawar, and S. Sagadevan, Ceram. Int. 50 (2024) 12121.
4. V. Kumari, K. Dey, S. Giri, and A. Bhaumik, RSC. Adv. 51 (2016) 45701.
5. J. He, S. Yang, and A. Riisager, Catal. Sci. Technol. 8 (2018) 790.
6. H.C. Shin, K.D. Jung, S.H. Han, J.W. Kim, and S.C. Choi, J. Ceram. Process. Res. 4 (2003) 30.
7. P.B. Kharat, S.D. More, S.B. Somvanshi, and K.M. Jadhav, J. Mater. Sci: Mater. Electron. 30 (2019) 6564.
8. J. Niresh, N. Archana, S. Neelakrishnan, V.M. Sivakumar, and D.S. Dharun, J. Ceram. Process. Res. 21 (2020) 343.
9. B. Liu, L. Zhang, K. Zhou, Z. Li, and H. Wang, Solid. State. Sci. 13 (2011) 1483.
10. K.S. Joshy, R. Augustine, A. Mayeen, S.M. Alex, A. Hasan, S. Thomas, and H. Chi, New. J. Chem. 44 (2020) 18162.
11. A.M. Ilosvai, D. Dojcsak, C. Váradi, M. Nagy, F. Kristály, B. Fiser, B. Viskolcz, and L. Vanyorek, Int. J. Mol. Sci. 23 (2022) 5081.
12. S. Pawar, M. Gandi, I. Arief, B. Krause, P. Pötschke, and S. Bose, Chemistry. Select. 21 (2017) 5984.
13. S. Hassan, M. Ahmad, A. Rehman, M.W. Iqbal, S.F. Shaukat, and H.S.M. Abd-Rabboh, J. Energy. Storage. 55 (2022) 105320.
14. E.M. Kamar, M. Khairy, and M.A. Mousa, J. Mater. Res. Technol. 24 (2023) 7381.
15. K. Anu and J. Hemalatha, Ceram. Int. 48 (2022) 3417.
16. B. Liu, M. Tang, X. Wei, and H. Li, J. Ceram. Process. Res. 23 (2022) 770.
17. Y. Zhang, Y. Yang, D. Chen, C. Chen, and Y. Meng, J. Ceram. Process. Res. 24 (2023) 342.
18. L.S. Chen, S.Y. Chen, and G.L. Lu, J. Mater. Sci. 41 (2006) 6465.
19. M.B. Shelar, P.A. Jadhav, S.S. Chougule, M.M. Mallapur, and B.K. Chougule, J. Alloy. Compd. 476 (2009) 760.
20. A.M. Abdeen, O.M. Hemeda, E.E. Assem, and M.M. El-Sehly, J. Magn. Magn. Mater. 238 (2002) 75.
21. S.S. Hussein and E.K. Al-Shakarchi, J. Ceram. Process. Res. 25 (2024) 323.
22. G.C. Kuczynski, Sintering Processes, Plenum Press, New York, 1980.
23. Y. Cheng, Y. Zheng, Y. Wang, F. Bao, and Y. Qin, J. Solid. State. Chem. 178 (2005) 2394.
24. I.N. Esha, Md. Al-Amin, F.T.Z. Toma, E. Hossain, M.N. I. Khan, and K.H. Maria, J. Ceram. Process. Res. 20 (2019) 530.
25. E.M.M. Ibrahim, Appl. Phys. A. 89 (2007) 203.
26. A.M. Abdeen, J. Magn. Magn. Mater. 192 (1999) 121-129.
27. R.S. Devan, Y.D. Kolekar, and B. Kchougule, J. Phys.: Condens. Matter. 18 (2006) 9809.
28. T. Mariam, I.N. Esha, M.N.I. Khan, S. Choudhury, and K.H. Maria, J. Ceram. Process. Res. 21 (2020) 442.
29. X.F. Chang, C. Zhang, X.L. Dong, W. Zhou, W.Q. Jin, Z.P. Shao, and N.P. Xu, J. Membrane. Sci. 316 (2008) 128.